Causality in real-time dynamic substructure testing

P.J. Gawthrop [a,1] S.A. Neild [b] A. Gonzalez-Buelga [b] D.J. Wagg [b]

[a] *Centre for Systems and Control and Department of Mechanical Engineering, University of Glasgow, GLASGOW. G12 8QQ Scotland.*

[b] *Department of Mechanical Engineering, Queens Building, University of Bristol, Bristol BS8 1TR, UK.*

Abstract

Causality, in the bond graph sense, is shown to provide a conceptual framework for the design of real-time dynamic substructure testing experiments. In particular, known stability problems with split-inertia substructured systems are reinterpreted as causality issues within the new conceptual framework.

As an example, causality analysis is used to provide a practical solution to a split-inertia substructuring problem and the solution is experimentally verified.

Key words: Substructuring; hardware-in-loop testing; causality; bond graphs.

1 Introduction

Real-time dynamic substructure testing is a hybrid numerical-experimental testing technique for simulating the dynamics of structures. It allows critical elements within a structure to be experimentally tested at full scale, whilst subjected to dynamic forcing. The structure under consideration is split into an experimental test piece (or *physical substructure*) and a numerical model describing the remainder of the structure (or *numerical substructure*). The challenge is to ensure that the physical and numerical substructures interact in real-time such that they emulate the behaviour of the complete structure during dynamic excitation.

Hybrid testing of large civil engineering structures subjected to extreme dynamic loading, such as earthquakes, has been successfully performed for many years at expanded time-scales (known as *pseudo-dynamic* testing [1–4]). For large structures,

[1] Corresponding author. Email: P.Gawthrop@eng.gla.ac.uk

a significant advantage of substructuring is that scaling effects can be eliminated as the portion of the structure being tested physically can be at full-scale. Due to the quasi-static nature of these expanded time-scale tests, a limitation is that dynamic and hysteretic forces must be estimated. Real-time tests, which allow the experimental testing of velocity-dependent characteristics, were first proposed by Nakashima et.al. [5]. Current real-time substructuring research falls broadly into two main areas; the development of numerical integration algorithms to compute the numerical model [6–8] and the development of control strategies to at the interface between the two substructures [9–12]. This paper is motivated from the control engineering approach, but has implications which span both areas of work. This is because the causality of a real-time dynamic substructure test is largely independent of both the control and numerical integration methods used. The causality is a property of how the two systems are *joined*, and where the division between numerical and physical is chosen. For many systems causal conflict can occur, with the result that the system can be unstable and/or un-implementable. By using a simple example, we seek to explain how causality in real-time dynamic substructuring is an essential concept which should be used in the design of all such tests.

Analysis of the system causality can be done in a number of ways. In this work the motivation comes from bond graphs [13–17], for which analytical and numerical methods for analysing causality have been established. Bond graph analysis has already been applied to real-time dynamic substructuring by Gawthrop, Wallace & Wagg [18], where the concept of a *virtual junction* between numerical and physical subsystems was developed. A introduction to causality and bond graphs is given by Gawthrop & Bevan [17] and an in-depth discussion of causality is given by Marquis-Favre & Scavarda [19]; In substructuring there are three main issues which relate to causality:

(1) The inclusion or exclusion of inertia, damping or elastic forces in either subsystem can affect the causality of the substructured model.
(2) The form of the numerical model will be determined by the causality substructured model. Ideally an ordinary differential equation form is sought rather than a differential-algebraic equation which is more difficult to implement numerically.
(3) The design of the *transfer system* (described in detail below), in particular the choice of force or displacement actuation, depends on the causality of the substructured model.

In some situations it is possible to have *causal conflict* which in substructuring usually indicates problems relating to items 1–3.

Causality and inversion are closely related [17]. In the linear case where systems can be represented as single-input, single-output transfer functions, bond graph results can be represented in block diagram terms. In particular, causality change corresponds to taking the reciprocal of the corresponding transfer function. As block

diagrams may be more familiar, results are interpreted in this way thoughout the paper. However, the bond graph approach is more general as it encompasses non-linear and multivariable systems as well; more importantly, although the block diagram is a useful way of presenting bond graph results, the results could not have been obtained as easily using block diagrams alone.

Substructuring involving split-mass systems is known to give rise to implementation problems [12, 20]. This paper provides a new causality-based conceptual framework for such systems as well as an experimentally-verified practical solution.

The purpose of this paper is to explain why causality is an important issue for real-time dynamic substructuring. Section 2.1 gives a causality-based framework for substructuring and gives illustrative examples. Section 4 focuses on situations where there is causal conflict and proposes a solution based on the design of a *coupling system*. Section 5 applies the methods to an experimental coupled pendulum oscillator system [20,21]; the range of experimental parameters is substantially increased using the new approach. Section 6 concludes the paper.

2 Substructuring and Causality

2.1 Substructuring

The physical and numerical substructures interact through the application of interface equilibrium and compatibility conditions. This may be achieved by measuring the force at the interface and imposing it on the numerical substructure within the numerical integration routine, hence satisfying the equilibrium condition. Then the interface displacement computed from the numerical model is imposed on the physical system, satisfiying the compatibility condition. A *transfer system* (typically an actuator) is required to impose the interface displacement calculated from the numerical substructure on the physical substructure. We refer to this substructuring configuration as *flow actuation* (adopting the bond graph terminology in which interactions between systems are thought of as efforts and flows). Alternatively, the measured interface displacement may be imposed on the numerical substructure and the resulting computed force imposed on the physical system. This configuration, in which the transfer system is required to impose the interface force, we term *effort actuation*.

For accurate recreation of the overall structural dynamics, real-time control errors at the interface between the numerical and physical substructures must be minimised. One of the most significant sources of error in substructuring comes from the effects of the transfer system (i.e. the actuator) dynamics. The transfer system is typically

a single electric or hydraulic actuator but may be more complex, for example an hydraulic shaking table [12]. Typically the actuator has an in-built or 'proprietary' controller, which is usually some form of PID control, and would provide a sufficient level of control for standard dynamic testing. However, in substructuring, there is a second feedback loop through the numerical model in addition to the controller feedback loop. The implication of the second feedback loop is that the control accuracy required for real-time substructuring is far greater than for standard dynamic testing. It is now well established that the proprietary controller is not sufficient to compensate for the actuator dynamics, particularly when testing lightly damped structures such as those typically found in civil engineering [7, 22, 23]. To reduce the effect of actuator dynamics, a range of control strategies which can be implemented as an *outer-loop* around the proprietary (*inner-loop*) controller have been proposed [10–12, 18, 22]. Gawthrop et.al [24] presented a technique to calculate the required control accuracy in terms of the maximum transfer system delay before system instability occurs. It has been observed that for lightly damped systems representative of those found in civil engineering this delay can be less than 1 ms [7].

For simplicity, we will assume that the transfer-system dynamics are linear and given by the transfer function $T_e(s)$ in the case of effort actuation and $T_f(s)$ in the case of flow actuation. As discussed previously [24], it is convenient to approximate these dynamics by a pure time-delay for the purposes of design.

2.2 Causal analysis of the ideal case

For a substructuring test where the compatibility condition is imposed on the physical substructure the actuator will need to be in displacement control and hence have a displacement feedback loop. In this case the equilibrium condition must be imposed on the numerical substructure and to achieve this the actuator force is measured and fed into the numerical substructure which in turn generates the displacement demand for the actuator – hence closing the second feedback loop. This combination of equilibrium and compatibility conditions ensures that the system is *causal*. It is possible to swap the conditions between the two subsystems, and still retain a causal system. However, it is also possible to propose a range of non-causal substructuring configurations. So the first observation we make is that a causal substructuring system arises naturally when a 'collocated' equilibrium-compatibility condition is used.

[Fig. 1 about here.]

To formalise this concept we consider the bond graph shown in Figure 1 which shows a substructured system where **Num** and **Phy** represent the *numerical* and *physical* substructures respectively. Both **Num** and **Phy** are assumed to have a

bond graph representation and are joined by a single bond representing the ideal coupling of the two subsystems (i.e. ignoring transfer system effects). Interactions between elements within a bond graph are defined in terms of an *effort* (which in this case is force) and *flow* (the bond graph convention is to use velocity however we will use displacement as this relates to our later analysis). In Figure 1, e_n denotes the numerical effort (force) and e_p the physical effort (force). Similarly the flows (displacements) are denoted f_n and f_p corresponding to the numerical and physical displacements respectively. In the ideal substructuring case $e_n = e_p$ and $f_p = f_n$, as denoted by the bond graph in Figure 1 [24]. In fact the bond graph formalises the concept of a collocated equilibrium-compatibility condition exactly by the effort and flow conditions defined on the bond. So the bond graph in Figure 1 represents the coupling of the two subsystems **Num** and **Phy** using the equilibrium condition $e_n = e_p$ and the compatibility condition $f_p = f_n$. There are two causality cases for the substructured system in Figure 1 corresponding to using either effort or flow actuation.

2.3 Choosing effort or flow actuation

The ideal case shown in Figure 1 ignores the transfer system but is useful to demonstrate the difference in causality between force (effort) and displacement (flow) actuation. This is shown in Figure 2 in both bond graph and block diagram form.

[Fig. 2 about here.]

Figure 2(a) shows the bond graph for effort (force) actuation and Figure 2(b) shows the case for flow actuation (displacement control). The two causality cases are distinguishable by the *causal stroke* (the vertical line drawn at one end of the bond) which indicates whether effort or flow is imposed on the subsystems joined by the bond — see [17] for further details. Each case can also be represented as a block-diagram representation. The block diagram of Figure 2(c) corresponds to Figure 2(a) and Figure 2(d) corresponds to Figure 2(b). In the block diagrams we have introduced transfer function representations of **Num** and **Phy** which are $N(s)$ and $P(s)$ respectively, where s is a complex scalar i.e. the Laplace domain variable. The subscripts e and f are used to denote whether the transfer functions $N(s)$ and $P(s)$ are defined for effort of flow causality respectively. It is important to note that the physical substructure (**Phy**) is typically strongly nonlinear and so a transfer function representation is not normally possible. However, it is useful in this context to analyse the closed loop system with (**Phy**) approximated by $P(s) + f(\cdot)$, where $f(\cdot)$ represents the some arbitrary nonlinear dynamics which will be neglected, without loss of generality, in some of our analysis.

The key observation to make from Figure 2 is that by changing the causality the transfer function blocks are effectively inverted (a more detailed discussion is given

by Gawthrop & Bevan [17]). In fact the relationship can be expressed as

$$N_f(s) = N_e^{-1}(s), \tag{1}$$
$$P_f(s) = P_e^{-1}(s). \tag{2}$$

As a result if the transfer functions are strictly proper (i.e. with relative degree ≥ 1) in one configuration then they will be improper in the other. In the later case causal conflict can occur, or the system could be non-causal. The examples shown later demonstrate that this causal conflict often manifests itself as a change from integral to derivative causality. A discussion on the problems associated with derivative causality can be found in [17].

2.4 Natural causality

In bond graph terms the *natural causality* of a system is that where the dynamic bond graph components **I** (representing masses) and **C** (representing springs) are in *integral causality* [17]: the block diagram equivalent is an integrator rather than a differentiator. In this case, the corresponding system transfer function is proper. In the sequel, we associate the proper transfer function $P(s)$ with **Phy** in natural causality and the proper transfer function $N(s)$ with **Num** in natural causality.

Implementing the system in it's natural causality will minimise problems associated with points 1– 3 and should be seen as an important part of preliminary substructuring design. The concept of natural causality (as we use it here) is not formalised beyond the conceptual, and we note that example systems can be configured in which natural causality either does not exist or alternatively is non-unique.

Defining a natural causality depends primarily on the definition of the substructuring problem, which includes point 1; the inclusion or exclusion of inertia, damping or elastic forces in either subsystem. In some cases, when defining the substructuring problem, there is a choice of how the system can be divided/coupled, and in this situation causality analysis can be used as a tool to ensure the system has a natural causality.

For simple systems, such as those considered in this paper, the causality analysis can be achieved by considering the proper/improper nature of the transfer functions. Alternatively the sequential causality assignment procedure (SCAP) [15, 17] developed for bond graph representations of the system can be used to assign integral causality to **I** and **C** components. In this work we will assume that systems are casual if the causality can be completed using SCAP, and we refer to this later as the SCAP assumption. Using SCAP has some other direct benefits. For example, the SCAP assumption implies that the entire system can be written in state-space form and therefore simulated numerically as an ordinary differential equation: a

differential-algebraic equation solver is not required. This resolves the issue raised in point 2.

3 Dividing the system: A mass-spring-damper example

The choice of which parts of the complete system are to form **Phy** and **Num** is often dictated by practical issues such as which particular component of the overall system needs to be tested. Beyond this there may be some flexibility in (i) choosing where to divide the system, and (ii) choosing whether to split a component between the substructures. In this section we consider a linear mass-spring-damper system which demonstrates the key concepts associated with the dividing/coupling process.

[Fig. 3 about here.]

[Table 1 about here.]

The mass-spring-damper system can be divided in a number of ways, and in Figure 3 the case is shown where **Phy** contains the spring and the numerical substructure **Num** contains the mass and damper. This division is shown schematically in Figure 3(a) and the corresponding bond graph is shown in Figure 3(b). The natural causality can be found either by using the bond graph, Figure 3(b), (using SCAP) or by examining the transfer functions. In this case the divided system corresponds to the causality of Figure 2(b) which corresponds to flow (i.e. displacement) actuation. This corresponds directly to the block diagram shown in Figure 2(d) and the transfer functions P_f and N_f are defined in the first row of Table 1 — see Gawthrop, Wallace & Wagg [18] for a more complete discussion of this system.

3.1 Splitting components

In this section we consider the consequences of splitting the spring between **Num** and **Phy** . This is achieved by using the parameter α to indicate the proportion of the component placed in **Num** . Having considered the case for splitting the spring we repeat the process for the damper and the mass.

We will use the concepts of *loop-gain* and *phase-margin* [25] to assess the robustness of the split component systems — see [24] for a discussion of these concepts applied to substructuring. Using the block diagrams of Figures 2(c) and 2(d), the loop-gains $L_e(s)$ and $L_f(s)$ are defined as the product of the two transfer functions

in the feedback loop respectively:

$$L_e(s) = N_e(s)P_e(s) \tag{3}$$
$$L_f(s) = N_f(s)P_f(s) \tag{4}$$

The loop gain and phase margin will be used for comparing cases for different α values.

3.1.1 Split spring

[Fig. 4 about here.]

[Table 2 about here.]

The case for the split spring is shown in Figure 4. The bond graphs in Figures 4(a) & 4(b), now indicate that the spring is divided in two parts, one in **Num** and the other in **Phy** . This system retains the original (integral) causality of the case when all the spring was in **Phy** . The corresponding transfer functions $N_f(s)$ and $P_f(s)$ (in the second row of Table 1) are proper.

The frequency response of the loop gain $L_f(s)$ (given by equation (4)) is shown in two forms. The Nyquist diagram shown in Figure 4(c) shows that stability margin increases with increasing α. This is expected, because when $\alpha = 1$ the system is entirely numerical, with no physical component, and so it will no longer be a sub-structured system. The modulus of the frequency response is shown in Figure 4(d), with the corresponding phase shown in Figure 4(e). This shows that the loop-gain goes to zero at high frequencies, indicating that high frequencies are attenuated. The phase margins ϕ_m measured from these plots give an indication of how robust the system is to delay (and other uncertainties) in the transfer system (as discussed in [24]). The variation of phase margin is shown in Figure 4(e) and summarised in Table 2 . As shown by the Nyquist diagram, the stability (i.e. phase) margin increases with increasing α.

3.1.2 Split damper

[Fig. 5 about here.]

[Table 3 about here.]

The situation here is similar to that of splitting the spring insofar as causality is unchanged. In contrast to the spring case, however, Figure 6 and Table 3 shows that phase margins are only slightly changed by splitting the damper.

3.1.3 Split mass

[Fig. 6 about here.]

[Table 4 about here.]

The split mass case is shown in Figure 6. This case is significantly different from the previous two cases. In this case the causality has changed from integral to derivative. This can be ascertained either from the bond graphs shown in Figures 6(a) & 6(b), or the transfer functions shown in (Table 1). Specifically, the physical part of the mass has *derivative* causality and $P_f(s)$ is improper.

As before the frequency response of the loop gain $L_f(s)$ is shown as both a Nyquist diagram, Figure 6(c) and as loop gain, Figure 6(d) and phase margin, Figure 6(e). The Nyquist diagram shows that stability margin increases with α. However, the loop gain shows that at high frequencies $L_f(s)$ does not go to zero but rather that $L_f(\infty) = \frac{\alpha}{1-\alpha}$. Thus if $\alpha > 0.5$, the phase margins, shown in Figure 6(e) reduce to zero and the system becomes unstable for an arbitrarily small phase delay in the transfer system.

In this discussion, flow actuation has been considered. In the case of the split-mass, switching to effort actuation does not resolve the restriction on α. From equations (1), (2), (3) and (4), it can be seen that the loop gain in effort actuation $L_e(s)$ is the inverse of the loop gain in flow actuation. Therefore, as with flow actuation, at high frequencies the loop gain does not tend to zero, resulting in the condition that if $\alpha < 0.5$ a small delay would induce instability. From a causality viewpoint, in the case of flow actuation the **Phy** transfer function is non-proper and in the case of effort actuation the **Num** transfer function is non-proper.

An approach to resolving this causal conflict is given in the next section.

4 System design to avoid causal conflict

[Fig. 7 about here.]

In the previous discussion, we have considered several ways in which causal conflict can occur; a typical example arises from splitting a mass component described in Section 3.1.3. However, in common with most forms of dynamic testing, substructuring need only be accurate within a limited frequency band . This fact can be exploited to resolve causal conflict by introducing a *coupling system*, **Cou** , into the substructured system. Typically this would be inserted between **Num** and **Phy** as indicated in Figure 7(a). This coupling system would be designed to gives strong coupling within the frequency band of interest, but weak coupling outside this range. In a range of cases, this approach can be used to resolve causal conflict.

In general, **Cou** is a two-port (and therefore two-input, two-output) system which, in the linear case would have four scalar transfer functions to describe it. Figures 7(b) and 7(c) give two simple special cases of **Cou** which, in the linear case, are associated with the single transfer function corresponding to the one-port subsystem **cou** . With the causality given, the version of Figure 7(b) imposes *effort* on both ports whereas the version of Figure 7(c) imposes *flow* on both ports. As discussed in Section 4.1, **cou** could, for example, represent a damped spring.

Figure 7(d) gives the block diagram corresponding to the bond graph of Figure 7(a) when using the version of **Cou** given in Figure 7(b) and, as discussed in Section 3, where $N(s)$, $C(s)$ and $P(s)$ are the transfer functions corresponding to **Num** , **cou** and **Phy** in natural causality.

[Fig. 8 about here.]

[Fig. 9 about here.]

A key observation is that Figure 7(d) shows *two* loops and there are, therefore, two loop gains. As discussed in Section 2.1, the loop gain is important when analysing robust stability of the substructured system. The question arises as to which loop is the relevant one in this case. As discussed previously [18, 24], it is the *transfer system*, providing the interface between numerical and physical substructures, which causes stability problems. Therefore it is the location of the transfer system **Tra** that determines the critical loop to consider. The two possibilities correspond to whether the transfer system generates flow or effort and lead to Figures 8 and 9 respectively. In each of these figures, (a) gives the bond graph of the substructured system with **Tra** included but without **Cou** , (b) gives the bond graph with **Cou** included and (c) and (d) give the corresponding block diagrams. We can now write down the expressions for the loop gain and the closed-loop frequency response (D) as

$$L_f = \frac{N}{P} \qquad D_f = \frac{NP}{N+P} \tag{5}$$

$$L_e = \frac{P}{N} \qquad D_e = D_f \tag{6}$$

$$L_p = \frac{CN}{1+CP} \qquad D_p = \frac{N(1+CP)}{1+C(N+P)} \tag{7}$$

$$L_n = \frac{CP}{1+CN} \qquad D_n = D_p \tag{8}$$

$$\tag{9}$$

Note that at those frequencies ω where $C(j\omega)$ is large:

$$L_n(j\omega) \approx L_f(j\omega) \tag{10}$$

$$L_p(j\omega) \approx L_e(j\omega) \tag{11}$$

$$D_n(j\omega) \approx D_f(j\omega) \tag{12}$$

In the case of Figure 7(b):

$$e_p = e_n = C_e(s)(f_n - f_p) \tag{13}$$

and in the case of Figure 7(c):

$$f_p = f_n = C_f(s)(e_n - e_p) \tag{14}$$

where $C_e(s)$ and $C_f(s)$ are the transfer functions corresponding to **cou** with effort and flow output respectively.

4.1 Example: Split mass system

[Fig. 10 about here.]

Split-mass systems are common in substructuring – see,for example, Neild et. al. [12]. The system used as an example in this section is a linearised version of a coupled oscillator-pendulum system which has been analysed previously [20, 21]; new experimental results appear in Section 5 of this paper. In particular, it was shown [21] that a key parameter is the ratio p of the two masses ($p = \frac{m_p}{m}$) and that stable substructuring requires $p < 1$. As will be shown in Section 4.1.1, this result is a direct consequence of causal conflict. With natural causality, the transfer functions corresponding to **Num** , **cou** and **Phy** respectively are:

$$N(s) = \frac{s}{ms^2 + c^s + k} \tag{15}$$

$$C(s) = \frac{c_c s + k_c}{s} \tag{16}$$

$$P(s) = \frac{1}{m_p s} = \frac{1}{pms} \tag{17}$$

The following subsections correspond to the bond graphs displayed in Figures 8(b) and 9(b) (with the block diagram equivalents of Figures 8(d) and 9(d) using the special coupling system **Cou** of Figure 7(b).

4.1.1 Flow actuation

[Fig. 11 about here.]

With reference to Figure 8(a), without **Cou** , there is causal conflict; either **Num** or **Phy** , but not both, has natural causality. With flow actuation, this leads to a loop gain given by (5)

$$L_f(s) = \frac{N}{P} = \frac{pms^2}{ms^2 + cs + k} \tag{18}$$

Setting $s = j\omega$ and letting $\omega \to \infty$, it follows that this loop gain has a constant high-frequency gain of p. Following the standard textbooks, this high-frequency gain must be less than unity for stability. This corresponds to the result of Gonzalez-Buelga et. al. [21]. Note that in the paper of Neild et. al. [12], $p = \frac{20}{100} = 0.2$.

However, from (7), inserting **Cou** gives the loop gain:

$$L_p = \frac{CN}{1+CP} = \frac{m_p s^2(c_c s + k_c)}{(m_p s^2 + c_c s + k_c)(ms^2 + cs + k)} \tag{19}$$

As L_p is proper, $\lim_{w\to\infty} L_p(j\omega) = 0$: the high-frequency gain is zero. This implementation implies that the transfer system **Tra** imposes flow onto the physical system; it must implement a form of *displacement* control.

In view of (19), it is convenient to reparameterise **Cou** in terms of natural frequency ω_c and damping ratio ξ_c when coupled to **Phy** :

$$k_c = m_p \omega_c^2 \tag{20}$$
$$c_c = 2 m_p \xi_c \omega_c \tag{21}$$

The implication of including **Cou** in **Phy** is that a *physical* spring must be attached between the physical mass m_p and the actuator. This idea has been previously suggested by [11].

[Fig. 12 about here.]

Alternatively, using elementary block-diagram manipulation on Figure 8(d), it follows that

$$e_p = \frac{C(s)T_f(s)}{1+C(s)P(s)} f_n = P^{-1}(s)T_f(s)\frac{C(s)P(s)}{1+C(s)P(s)} f_n \tag{22}$$

The latter form of the equation corresponds to Figure 12 and can thus be implemented *numerically*. In particular, using (16) and (17), the required filter is:

$$\frac{C(s)P(s)}{1+C(s)P(s)} = \frac{c_c s + k_s}{m_p s^2 + c_c s + k_s} \tag{23}$$

However, this formulation is based on the assumption that **Phy** is linear with a known transfer function $P(s)$. If these assumptions do not hold then the implementation of Figure 12 is an *approximation* to the implementation of Figure 8(d).

4.1.2 Effort actuation

[Fig. 13 about here.]

The use of flow actuation (Section 4.1.1) leads to either the physical implementation of the coupling system **Cou** or an approximate numerical implementation. An alternative approach is to use effort actuation and implement **Cou** numerically.

With reference to Figure 9(a), without **Cou** , there is causal conflict; either **Num** or **Phy** , but not both, has natural causality. With effort actuation, this leads to a loop gain given by (6)

$$L_e(s) = \frac{P}{N} = L_f^{-1}(s) = \frac{ms^2 + cs + k}{pms^2} \tag{24}$$

This loop gain has a constant high-frequency gain of $\frac{1}{p}$. Once again, this constant high-frequency gain is undesirable; however, from (8), inserting **Cou** gives the loop gain:

$$L_n = \frac{CP}{1+CN} = \frac{(c_c s + k_c)(ms^2 + cs + k)}{m_p s^2(ms^2 + (c+c_s)s + (k+k_c))} \tag{25}$$

As L_n is proper, $\lim_{w\to\infty} L_n(j\omega) = 0$: the high-frequency gain is zero.

This implementation implies that the transfer system **Tra** imposes effort onto the physical system; it must implement a form of *force* control.

With reference to Figure 9(d), the force control represented by the transfer system $T_f(s)$ is embedded within a feedback loop involving $P(s)$ and $C(s)$. In control system terms, $T_e(s)$ represents an inner-loop, $C(s)$ a controller and $P(s)$ a system. The interpretation of the bond graph representing $C(s)$ as a controller is explored in [17, Figure 11].

5 Experimental Results

[Fig. 14 about here.]

The experimental system is shown in Figure 14. This system has been discussed previously [20, 21] and analysed in terms of its equations of motion linearised about the vertical down pendulum position. As the purpose of the experiment is to examine non-linear system behaviour for a range of parameters, it is advantage to have as wide range of parameters as possible. A key parameter is the mass ratio $p = \frac{m}{M}$, which represents the ratio of the pendulum mass, m to the mass-spring-damper mass, M. It is usual to consider this system when the mass ratio $p < 1$, such that the pendulum is driven by the mass-spring-damper, leading to autoparametric resonance phenomena. When $p > 1$, the situation is reversed and the inertia from the pendulum mass drives the mass-spring-damper. In previous substructuring tests only the $p < 1$ case could be simulated. A detailed analysis of why the $p > 1$ is unstable is given by Kyrychko et. al. [20].

[Fig. 15 about here.]

In this section, a redesign of the substructuring experiment based on the causality reasoning of Section 4.1 will allow the range of parameter p to be increased to include values of $p > 1$. As in the previous work, this analysis is based on a linearised system model and results presented in this section show experimentally that the predicted enhanced parameter range is experimentally feasible when applied to the actual non-linear system.

The experimental setup used was the same as that reported by [21] except that the *coupling system* **Cou** is included in the form of (23) of Section 4.1.1. The excitation to the system is via a force $F_e = \alpha \sin(\omega_e t)$, acting on the mass-spring-damper system. See figure 14. Two different sets of experiments were developed: in the first ones we show that it is possible to conduct substructuring tests when $p > 1$. In the second ones we study their accuracy. As in [21], it is useful to express results in terms of the effective delay τ leading to instability. In particular we define

$$\tau_c = \frac{\phi_m}{\omega_m} \tag{26}$$

where ϕ_m is the phase margin and ω_m the corresponding frequency, such that τ_c represents the *critical* delay value at which the system goes unstable. This phenomena has been demonstrated using experimental substructuring tests, for example in [21, Figure 6], where experimental and theoretical results showing the stability boundary of the substructured relating $p = \frac{m}{M}$ to delay τ are shown.

Previous experiments had shown that the actuator had an effective delay of $\tau_a = 0.025$sec. In order to locate the stability boundary an additional variable numerical delay, τ_n was added during the tests. Different p ratios where tested by changing the pendulum bob (m). For each value of p shown in Figure 15, the delay $\tau = \tau_a + \tau_n$ was increased until the onset of instability at $\tau = \tau_c$. Results for two different ω_c values are shown in Figure 15. As can be seen from Figure 15(a), an experimental value of $p = 1.65$ was reached. For comparison, the highest experimental value reported in [21, Figure 6.] was about $p = 0.6$. Because of the built in actuator delay ($\tau_a = 0.025$sec), it was not possible to reduce τ further than shown. It's important to note that, despite the limitations of the experiment, the theoretical curve becomes asymptotic to the p axis as $p \to \infty$, whereas without the coupling system the curve terminates at the $p = 1$ point [20, 21]. So the effect of introducing the coupling system in this case is (i) to increase the stable zone of operation for the substructuring system, and (ii) to allow the $p > 1$ case to be simulated.

In the second set of experimental hybrid tests, to highlight the significance of the improvement achieved, we have performed experimental substructuring simulations of the stability boundary of the semitrivial solution (the downward vertical position of the pendulum is stable) in the $\alpha - \hat{\omega}$ parameter space. α is the magnitude of the external excitation and $\hat{\omega} = \frac{\omega_e}{2\omega_p}$, the ratio between external excitation

frequency and twice the pendulum frequency.

The stability boundary marked 'Theory' in Figure 16 corresponds to a line of subcritical Hopf bifurcations. Above this line the downward vertical pendulum position becomes unstable [26]. In the previous work, [21], this was carried out for $p = 0.1$, and $p = 1$ was not possible. The results shown in Figure 16 are produced using the coupling system with $p = 1$.

[Fig. 16 about here.]

A clear resonance can be seen at $\hat{\omega} = 1$, with the stable zone being below the data lines. There is a good correlation between experimental substructuring results and the theoretical curve.

6 Conclusion

Building on the bond graph framework of Gawthrop et. al. [18], the causality attribute of the bond graph approach has been used to examine issues of substructuring arising when components are split between the numerical and physical substrucures. The concept of a *coupling system* has been introduced and shown to overcome problems arising when a mass is split. A set of experiments reported by Gonzalez-Buelga et. al. [21] is redesigned using the coupling system concept and rerun with parameter values not previously compatible with stability of the substructured system.

References

[1] F. Molina, S. Sorace, G. Terenzi, G. Magonette, B. Viaccoz, Seismic tests on reinforced concrete and steel frames retrofitted with dissipative braces, Earthquake Engng Struc. Dyn. 33 (2004) 1373–1394.

[2] P. Shing, S. Mahin, Seismic tests on reinforced concrete and steel frames retrofitted with dissipative braces, Earthquake Engng Struc. Dyn. 15 (1987) 409–424.

[3] J. Donea, G. Magonette, P. Negro, P. Pegon, A. Pinto, G. Verzeletti, Pseudodynamic capabilities of the elsa laboratory for earthquake testing of large structures., Earthquake Spectra 12 (1996) 163–180.

[4] O. Bursi, P. Shing, Evaluation of some implicit time-stepping algorithms for pseudodynamic tests, Earthquake Engng Struc. Dyn. 25 (1996) 333–355.

[5] Nakashima, H. Kato, E. Takaoka., Development of real-time pseudo dynamic testing, Earthquake Engng Struc. Dyn. 21 (1992) 779–792.

[6] A. Blakeborough, M. Williams, A. Darby, D. Williams, The development of real-time substructure testing., Philosophical Transactions of the Royal Society pt. A 359 (1869-1891).

[7] P. Bonnet, C. Lim, M. Williams, A. Blakeborough, S. Neild, D. Stoten, C. Taylor., Real-time hybrid experiments with newmark integration, mcsmd outer-loop control and multi-tasking strategies, Earthquake Engng Struc. Dyn. 36 (2007) 119–141.

[8] O. Bursi, A. Gonzalez-Buelga, S. Neild, L. Vulcan, D. Wagg, Novel partitioned rosenbrock-based algorithms for real-time dynamic substructure testing, Earthquake Engng Struc. Dyn. xx (2007) xx.

[9] A. P. Darby, A. Blakeborough, M. S. Williams, Improved control algorithm for real-time substructure testing, Earthquake Engng Struc. Dyn. 30 (3) (2001) 431–448.

[10] M. Wallace, J. Sieber, S. Neild, D. Wagg, B. Krauskopf, A delay differential equation approach to real-time dynamic substructuring, Earthquake Engng Struc. Dyn. 34 (15) (2005) 1817 – 1832.

[11] A. Reinhorn, M. Sivaselvan, Z. Liang, X. Shao, Real-time dynamic hybrid testing of structural systems., in: Thirteenth World Conference on Earthquake Engineering, Vancouver, 2004, paper No 1644.

[12] S. Neild, D. Stoten, D.Drury, D.J.Wagg, Control issues relating to real-time substructuring experiments using a shaking table, Earthquake Engng Struc. Dyn. 34 (2005) 1171–1192.

[13] F. E. Cellier, Continuous system modelling, Springer-Verlag, 1991.

[14] P. J. Gawthrop, L. P. S. Smith, Metamodelling: Bond Graphs and Dynamic Systems, Prentice Hall, Hemel Hempstead, Herts, England., 1996.

[15] D. Karnopp, D. L. Margolis, R. C. Rosenberg, System Dynamics : Modeling and Simulation of Mechatronic Systems, 3rd Edition, Horizon Publishers and Distributors Inc, 2000.

[16] A. Mukherjee, R. Karmakar, A. Samantaray, Bond Graph in Modeling, Simulation and Fault Detection, I.K. International Publishing, New Delhi, 2006.

[17] P. J. Gawthrop, G. P. Bevan, Bond-graph modeling: A tutorial introduction for control engineers, IEEE Control Systems Magazine 27 (2) (2007) 24–45.

[18] P. Gawthrop, M. Wallace, D. Wagg, Bond-graph based substructuring of dynamical systems, Earthquake Engng Struc. Dyn. 34 (6) (2005) 687–703.

[19] W. Marquis-Favre, S. Scavarda, Alternative causality assignment procedures in bond graph for mechanical systems, Journal of Dynamic Systems, Measurement and Control, Transactions of the ASME 124 (2002) 457–463.

[20] Y. Kyrychko, K. Blyuss, A. Gonzalez-Buelga, S. Hogan, D. Wagg, Real-time dynamic substructuring in a coupled oscillator-pendulum system, Proceedings of the Royal Society A 462 (2068) (2006) 1271 – 1294.

[21] A. Gonzalez-Buelga, D. Wagg, S. A. Neild, Parametric variation of a coupled pendulum-oscillator system using real-time dynamic substructuring, Structural Control and Health Monitoring xx (xx) (2007) xx, published on-line 17 Oct 2006.

[22] A. Darby, M. Williams, A. Blakeborough, Stability and delay compensation for real-time substructure testing, ASCE Journal of Engineering Mechanics 128 (2002) 1276–1284.

[23] C. Lim, S. Neild, D. Stoten, D. Drury, C. Taylor, Adaptive control strategy for dynamic substructuring tests, ASCE Journal of Engineering Mechanics xx (2007) xx.

[24] P. Gawthrop, M. Wallace, S. Neild, D. Wagg, Robust real-time substructuring techniques for under-damped systems, Structural Control and Health Monitoring 14 (4) (2007) 591–608, published on-line: 19 May 2006.

[25] G. Goodwin, S. Graebe, M. Salgado, Control System Design, Prentice Hall, 2001.

[26] A. Tondl, T. Ruijgrok, F. Verhulst, R. Nabergoj, Autoparametric resonance in mechanical systems, Cambridge University Press, Cambridge, 2000.

List of Figures

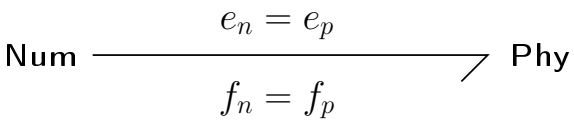

Fig. 1. Bond graph interpretation of substructuring. **Num** is the *numerical* substructure (implemented in software) and **Phy** is the physical substructure. The bond linking **Num** and **Phy** carries an effort (typically a force) and a flow (typically a velocity).

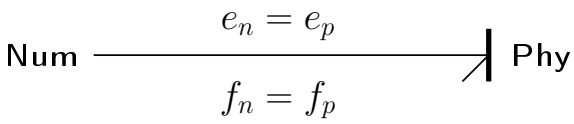

(a) Effort actuation: bond graph

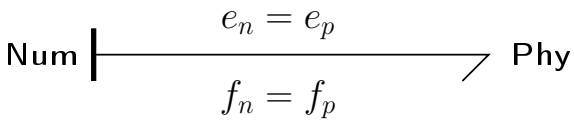

(b) Flow actuation: bond graph

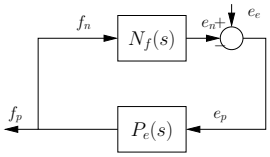

(c) Effort actuation: block diagram

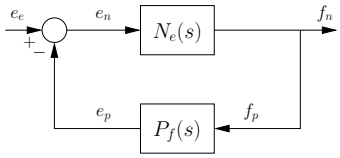

(d) Flow actuation: block diagram

Fig. 2. Bond graph Causality. (a) The causal stroke indicates that effort is imposed on **Phy** and flow is imposed on **Num** ; this corresponds to *force* actuation. (b) The causal stroke indicates that flow is imposed on **Phy** and effort is imposed on **Num** ; this corresponds to *position* actuation. (c) The block diagram corresponding to the bond graph of (a). (d) The block diagram corresponding to the bond graph of (b). Note that $N_e = N_f^{-1}$ and $P_e = P_f^{-1}$. In (c) and (d) an external effort has been added for later use corresponding to an external force acting on **Num** .

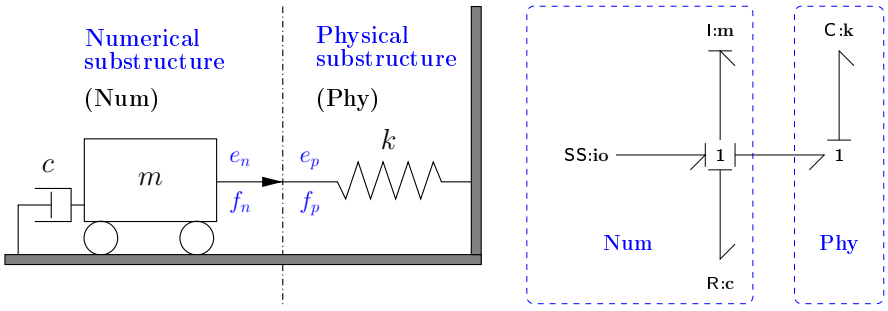

(a) Schematic (b) Bond graph

Fig. 3. A mass-spring-damper system. (a) The schematic diagram shows a mass-spring–damper system substructures so that **Num** comprises the mass and damper and **Phy** the spring. (b) The bond graph corresponding to (a) has been divided in Figure 1. It is assumed that an external force is applied to **Num** via the **SS** component.

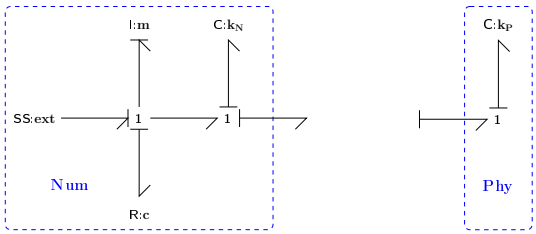

(a) Num

(b) Phy

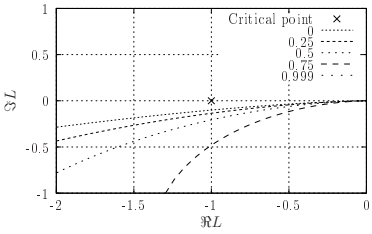

(c) Nyquist diagram

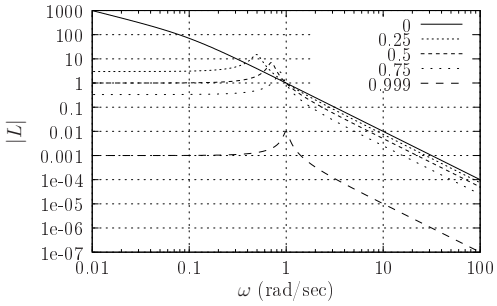

(d) Loop gain $|L(j\omega)|$

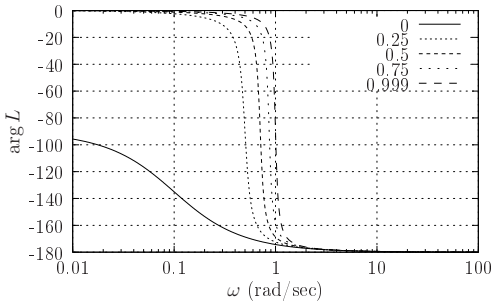

(e) Loop phase $\arg L(j\omega)$

Fig. 4. Split spring: $k_N = \alpha k$, $k_P = (1-\alpha)k$, $k = m = 1$, $c = 0.1$. Unlike Figure 3, the spring (the bond graph **C**:**c**omponent) has been split between **Num** and **Phy** ; in this case, causality is not changed. (c) The Nyquist diagram indicates that the stability margin increases with α, numerical values appear in Table 2.

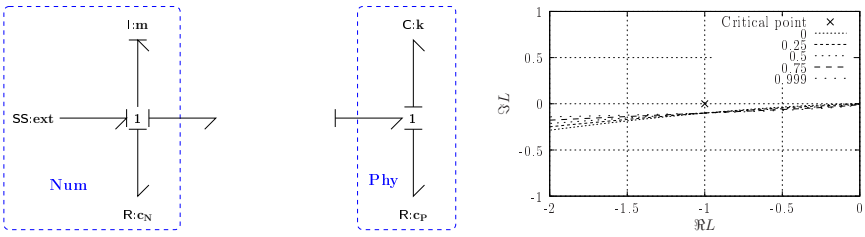

(a) Num (b) Phy (c) Nyquist diagram

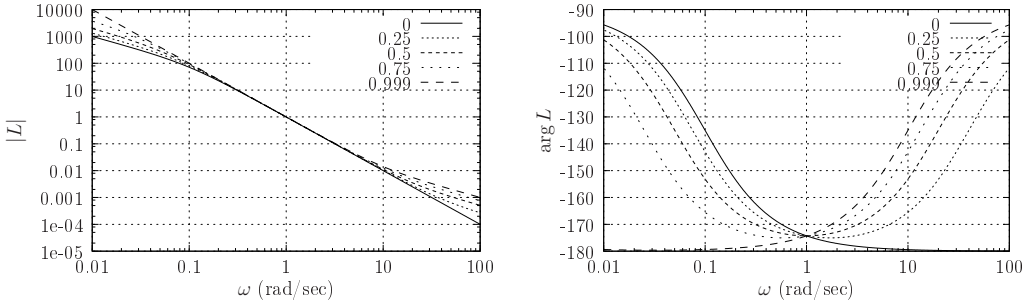

(d) Loop gain $|L(j\omega)|$ (e) Loop phase $\arg L(j\omega)$

Fig. 5. Split damper: $c_N = (1-\alpha)c$, $c_P = \alpha c$, $k = m = 1$, $c = 0.1$. Unlike Figure 3, the damper (the bond graph **R**:**c**omponent) has been split between **Num** and **Phy** ; in this case, causality is not changed. (c) The Nyquist diagram indicates that the stability margin is unchanged with α, numerical values appear in Table 3.

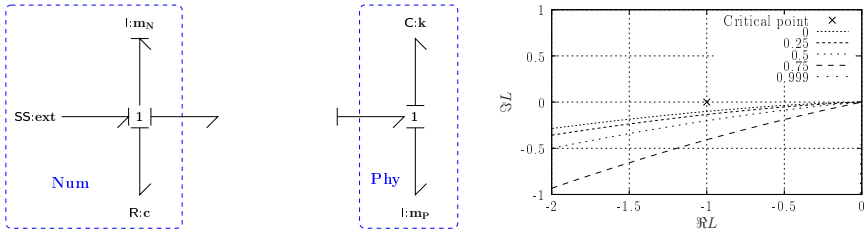

(a) Num (b) Phy (c) Nyquist diagram

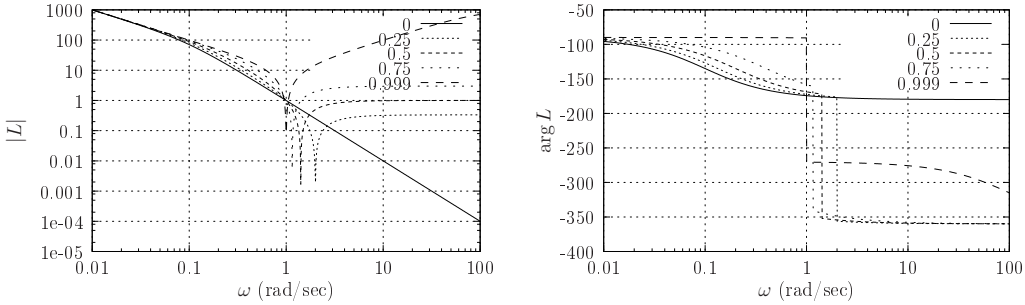

(d) Loop gain $|L(j\omega)|$ (e) Loop phase $\arg L(j\omega)$

Fig. 6. Split mass: $m_N = (1-\alpha)m$, $m_P = \alpha m$, $k = m = 1$, $c = 0.1$. Unlike Figure 3, the mass (the bond graph **I**:**c**omponent) has been split between **Num** and **Phy** ; in this case, causality is changed: one of the **I**:**m**ust have *derivative* causality. (c) The Nyquist diagram does not tell the full story in this case as the derivative causality leads to a non-zero loop gain at high frequencies ($L(j\infty) \neq 0$). (d). Although the system of Figure 3 ($\alpha = 0$) gives a loop gain with zero gain at high frequencies, this is not the case for $\alpha > 0$ as $L(j\infty) = \frac{\alpha}{1-\alpha}$. In particular, when $\alpha > 0.5$, $L(j\infty) > 1$ leading to zero stability margins

.

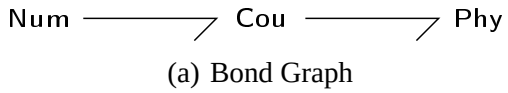

(a) Bond Graph

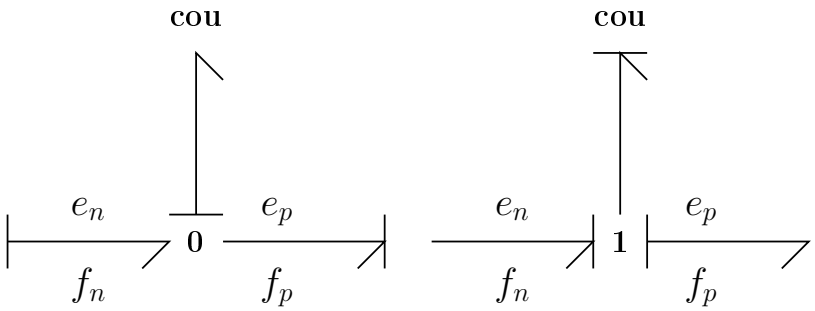

(b) Effort-imposing **Cou** (c) Flow-imposing **Cou**

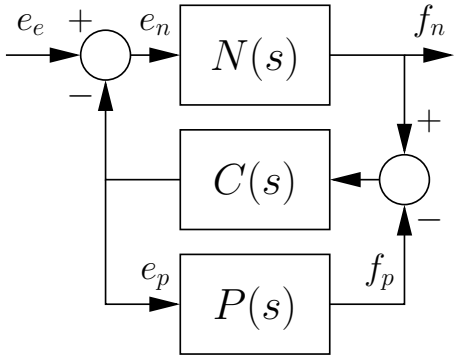

(d) Block Diagram

Fig. 7. Avoiding Causal Conflict using a coupling system **Cou** . (a) **Cou** is interposed between **Num** and **Phy** of Figure 6. (b) and (c) are special forms of **Cou** imposing effort and flow respectively. (c) gives the block diagram corresponding to (b) where $N(s)$, $C(s)$ and $P(s)$ are the transfer functions corresponding to **Num** , **cou** and **Phy** in natural causality. Note that **Cou** creates *two* feedback loops.

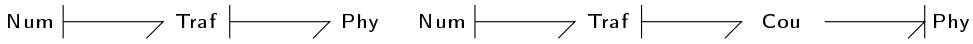

(a) No coupling system: Bond Graph

(b) **Cou** in **Phy** : Bond Graph

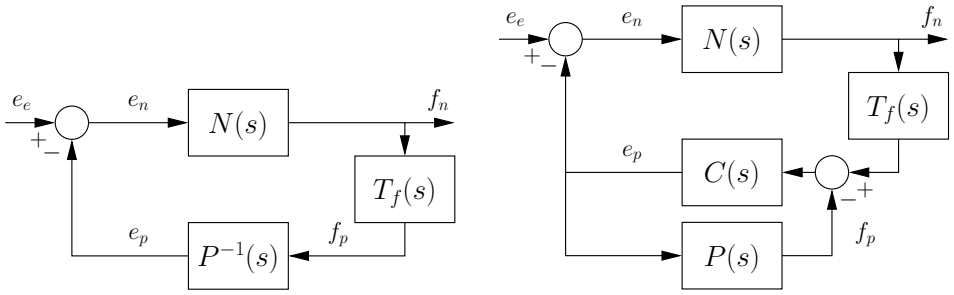

(c) No coupling system: block diagram

(d) **Cou** in **Phy** : block diagram

Fig. 8. Coupling system: flow actuation. (a) and (b) give the bond graph representation without and with a coupling system; note that the causality of **Phy** changes when the coupling system is added. (c) and (d) give the corresponding block diagrams. **Traf** is the flow actuation version of the transfer system **Tra** associated with the transfer function $T_f(s)$

(a) No coupling system: Bond Graph

(b) **Cou** in **Num** : Bond Graph

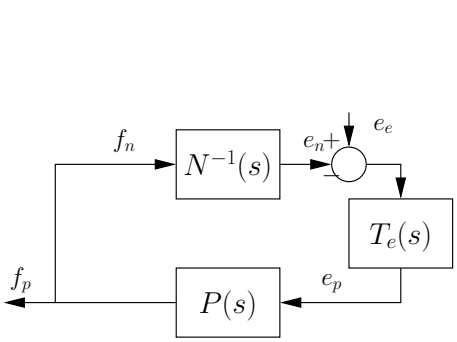

(c) No coupling system: block diagram

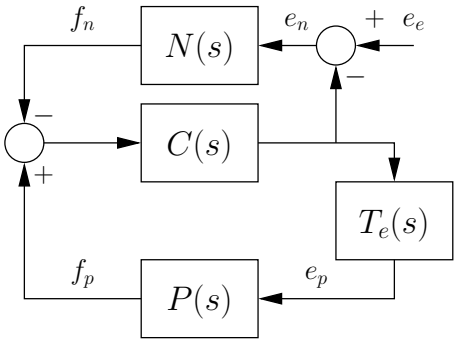

(d) **Cou** in **Num** : block diagram

Fig. 9. Coupling system: effort actuation. (a) and (b) give the bond graph representation without and with a coupling system; note that the causality of **Num** changes when the coupling system is added. (c) and (d) give the corresponding block diagrams. **Trae** is the effort actuation version of the transfer system **Tra** associated with the transfer function $T_e(s)$

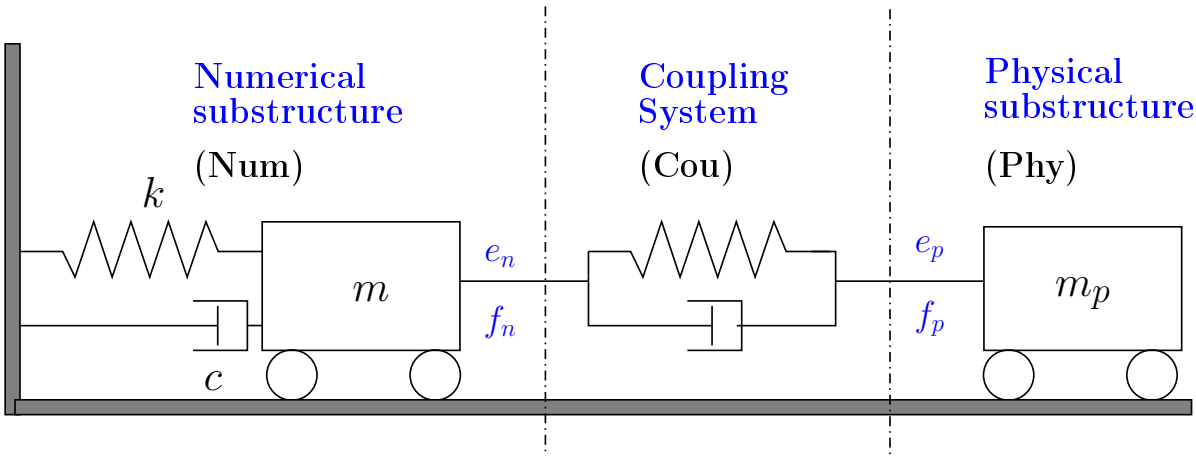

(a) Schematic

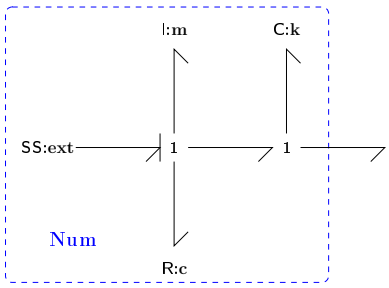

(b) **Num**

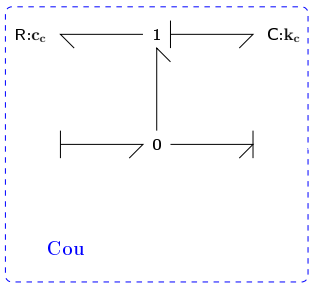

(c) **Cou**

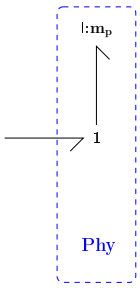

(d) **Phy**

Fig. 10. Split-mass system: bond graph. (a) shows the schematic diagram of a mass-spring–damper system. (b) Shows the numerical system **Num** : a mass-spring-damper oscillator (c) shows the coupling system **Cou** of Figure 7(b) which corresponds to a damped spring. (d) **Phy** is an inertia with mass m_p represented by **I:$\mathbf{m_p}$**. A key parameter is $p = \frac{m_p}{m}$.

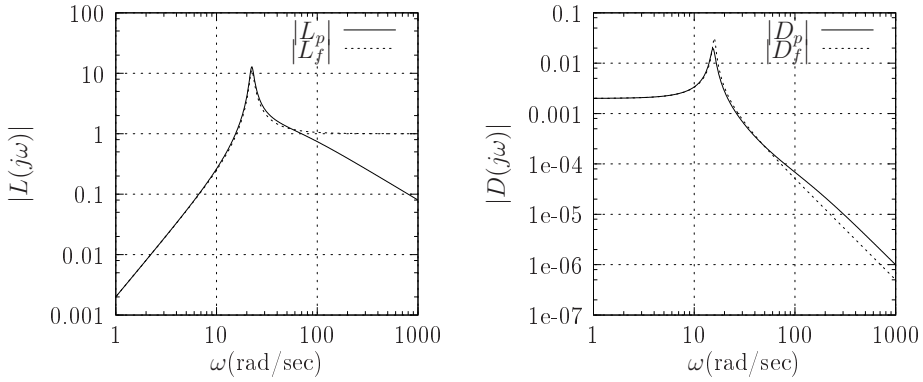

(a) Loop gain L_p and L_f (b) Closed-loop D_p and D_f

Fig. 11. Frequency responses: flow actuation. $m = 1$kg, $c = 2$kg/sec, $k = 500$N/m, $m = 1$kg, $\xi_c = 1$, $\omega_c = 20$rad/sec. (a) The Magnitude of the loop gains L_p (Figure 8(b)) and L_f (Figure 8(a)); $|L_f(j\infty)| = 1$, but **Cou** ensures that the loop-gain L_p is small at high frequencies. (b) Closed-loop frequency response $|D(j\omega)|$ **Cou** leads to a discrepancy above about 20rad/sec

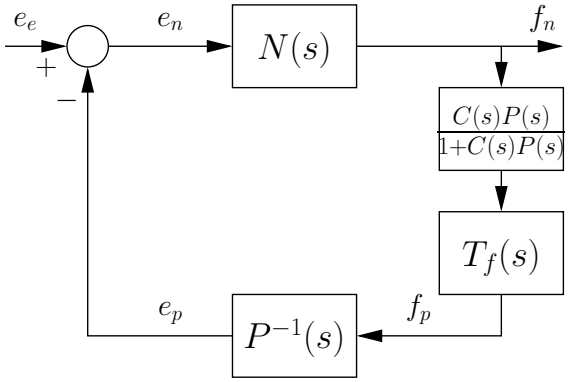

Fig. 12. Approximate numerical implementation

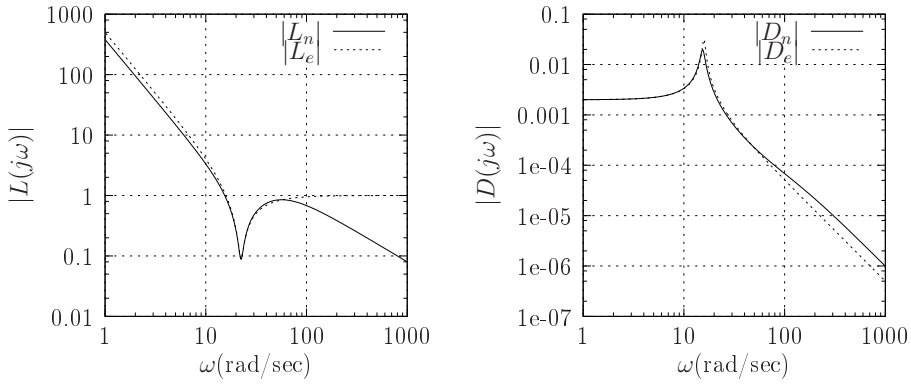

(a) Loop gain L_n and L_e (b) Closed-loop D_n and D_e

Fig. 13. Frequency responses: effort actuation. The parameters are the same as in Figure 11. (a) The Magnitude of the loop gains L_n (Figure 9(b)) and L_e (Figure 9(a)); $|L_e(j\infty)| = 1$, but **Cou** ensures that the loop-gain L_e is small at high frequencies. (b) Closed-loop frequency response $|D(j\omega)|$ **Cou** leads to a discrepancy above about 20rad/sec

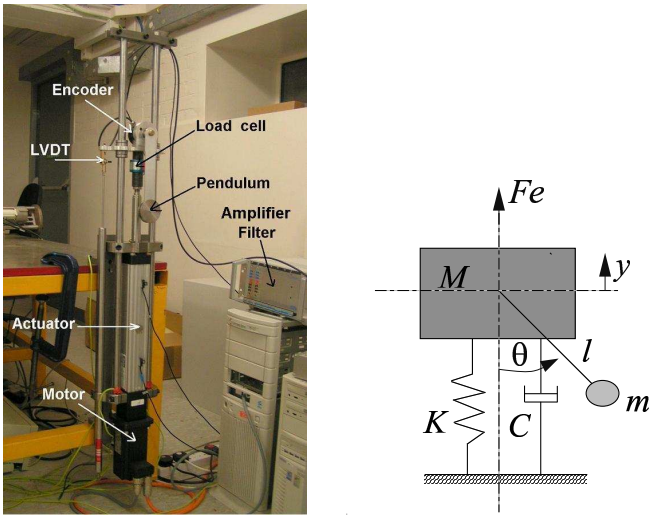

(a) Photograph (b) Schematic Diagram

Fig. 14. Experimental Pendulum-Oscillator System

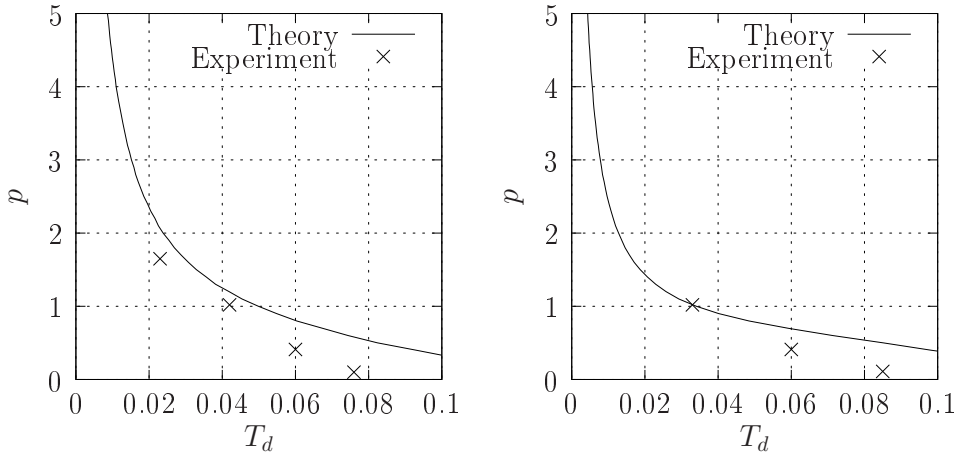

(a) p-T_m diagram: $w_c = 20$ (b) p-T_m diagram: $w_c = 40$

Fig. 15. Experimental results. (a),(b) give experimental measurements of the onset of instability compared with theoretical values for the linear case this corresponds to [21, Fig. 6] but with larger mass-ratio p.

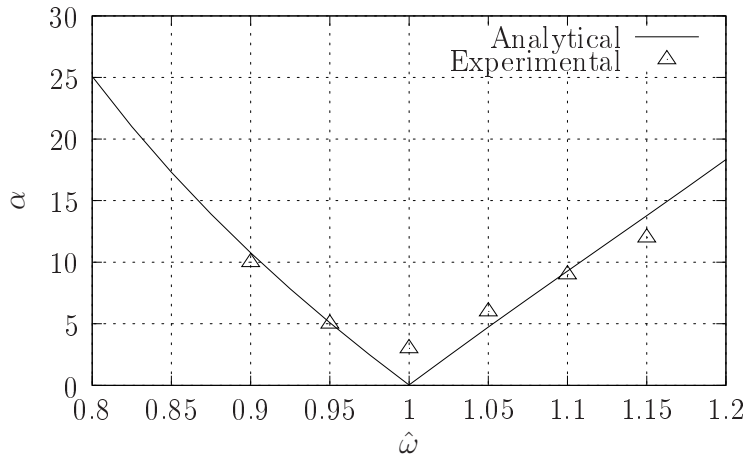

Fig. 16. Experimental results. Experimental measurements of the onset of instability of the coupled pendulum-oscillator system – corresponds to [21, Fig. 10a] but with mass ratio increased from $p = 0.1$ to $p = 1$.

List of Tables

Split	$N_f(s)$	$P_f(s)$
Between spring and mass	$\frac{1}{ms+c}$	$\frac{k}{s}$
Within spring	$\frac{s}{ms^2+cs+\alpha k}$	$\frac{(1-\alpha)k}{s}$
Within damper	$\frac{1}{ms+(1-\alpha)c}$	$\frac{\alpha cs+k}{s}$
Within mass	$\frac{1}{(1-\alpha)ms+c}$	$\frac{\alpha ms^2+k}{s}$

Table 1
Substructure Transfer Functions

α	ϕ_m (deg)	T_m (ms)
0.0	5.7	100
0.2	7.7	134
0.5	11.8	208
0.8	23.9	422
1.0	∞	∞

Table 2
Split spring: stability margins

α	ϕ_m (deg)	T_m (ms)
0.0	5.7	100
0.2	5.7	100
0.5	5.7	100
0.8	5.7	100
1.0	5.7	99

Table 3
Split damper: stability margins .

α	ϕ_m (deg)	T_m (ms)
0.0	5.7	100
0.2	7.6	133
0.5	0	0
0.8	0	0
1.0	0	0

Table 4
Split mass: stability margins